

Article

Performance and Life Degradation Characteristics Analysis of NCM LIB for BESS

Soon-Jong Kwon ¹, Sung-Eun Lee ², Ji-Hun Lim ² , Jinhyeok Choi ² and Jonghoon Kim ^{1,*} 

¹ Department of Electrical Engineering, Chungnam National University, Daejeon 34134, Korea; ksj9169@nate.com

² Korea Electric Power Corporation Research Institute, Daejeon 34056, Korea; sungeun.lee@kepco.co.kr (S.-E.L.); thedayseye@kepco.co.kr (J.-H.L.); renahren@kepco.co.kr (J.H.C.)

* Correspondence: whdgns0422@cnu.ac.kr or qwzxs@hanmail.net; Tel.: +82-42-821-5657

Received: 22 November 2018; Accepted: 4 December 2018; Published: 7 December 2018



Abstract: The battery energy storage system (BESS) market is growing rapidly around the world. Lithium Nickel Cobalt Manganese Oxide (LiNiCoMnO₂) is attracting attention due to its excellent energy density, high output power, and fast response characteristics. It is being extensively researched and is finding use in many applications, such as in electric vehicles (EV) and energy storage systems (ESS). The performance and lifetime characteristics of a battery change for varying Ni contents. The consideration of these characteristics of a battery allow for a more reliable battery management system (BMS) design. In this study, various experiments and analyses were carried out using a lithium-ion battery (NCM LIB) with differing Ni contents. In particular, the following two combinations were studied: LiNi_{0.5}Co_{0.2}Mn_{0.3}O₂ (NCM523) and LiNi_{0.6}Co_{0.2}Mn_{0.2}O₂ (NCM622). Various analyses were performed, such as C-rate (C-rate is the charge-discharge rate of a battery relative to nominal capacity) performance tests, hybrid pulse power characterization (HPPC), accelerated deterioration experiments, electrochemical impedance spectroscopy (EIS), parameter estimations of battery equivalent circuits through alternating current (AC) and direct current (DC) impedance, and comparative analyses of battery modeling.

Keywords: performance and life characteristics analysis of NCM LIB; hybrid pulse power characterization (HPPC); accelerated deterioration experiment; electrochemical impedance spectroscopy (EIS); parameter estimation; battery model using ECM

1. Introduction

An energy storage system (ESS) is a system that stores surplus power and supplies that produce power when needed to improve power efficiency. There are various types of ESS such as pumped hydro storage (PHS), flywheel energy storage (FES), compressed air energy storage (CAES), and battery energy storage systems (BESS) [1–5]. Among these, BESS refers to a type of ESS that stores and supplies energy by using oxidation/reduction reactions involving ions. BESS has been used in various applications due to its high energy density and efficiency, its applicability, and its fast charge/discharge response characteristics.

Types of BESSs can be divided into several broad categories, including Lead-acid batteries, NiCd (Nickel Cadmium) batteries, NiMH (Nickel Metal Hydride) batteries, Li-ion batteries (LIBs), NaS (Sodium Sulfur) batteries, and supercapacitors. These batteries possess various performance and lifetime characteristics. For example, supercapacitors can provide more output power and a more stable lifetime performance than other batteries. However, the problem of poor energy density needs to be solved. Among these categories, lithium-ion batteries charge and discharge energy using a reversible oxidation/reduction reaction of lithium-ions [1–5]. As concerns about the depletion of

fossil fuels and global environmental pollution have increased, much research and development is being conducted towards the potential application of a secondary lithium-ion battery to hybrid electric vehicles, plug-in hybrid electric vehicles, and full electric vehicles. In addition, LIBs predominate as a component of the power grid ESS. There are various driving forces for ESS application in the power grid, such as frequency regulation (maintaining system frequency at an acceptable level in a large power grid), grid reliability (improved through the incorporation of renewable energy sources), and peak reduction (used primarily by end users to reduce electricity bills). The global BESS market is growing rapidly. Global LIB shipments, which were aggregated to 544.2 GWh in 2015, are expected to grow to 764 GWh by 2020 [2].

Batteries account for a large portion of the cost of BESS, a market sector that is expected to expand more rapidly due to the expansion of the electric vehicle market and the increasing use of renewable energy sources. Therefore, a more precise understanding of battery technology will lead to reductions in cost due to the extension of battery life. State of health (SOH), the condition of the battery that essentially equates to battery life, decreases steadily for various reasons as a battery is used. Understanding battery degradation characteristics can prevent accidents, such as fire and explosion, due to battery misuse and/or excessive use. The performance, impedance, and lifetime characteristics of a battery with different composition ratios were thus analyzed at each C-rate as part of this study.

2. Oxide-Based Cathode Material (Lithium-Ion Battery)

Figure 1 shows the theoretical capacity and potential range of various cathode materials used in LIB. LiCoO_2 (LCO), a layered structure, has been used as a cathode active material in lithium-ion secondary batteries from the very beginning of LIB commercialization. This material remains the mainstay of cathode active materials. However, the cobalt (Co) used in LCO is a rare-earth metal that is found in only small global reserves and suffers from supply instability due to its concentration in a specific region. Therefore, as shown in Table 1, cathode materials with various properties have been developed. LiNiO_2 (LNO) is a layered structure, LiMn_2O_4 (LMO) is a spinel structure, and LiFePO_4 (LFP) is an olivine structure. These alternative representative cathode materials make use of Ni, Mn, and Fe, which are all elements with a relatively high supply stability [1–4].

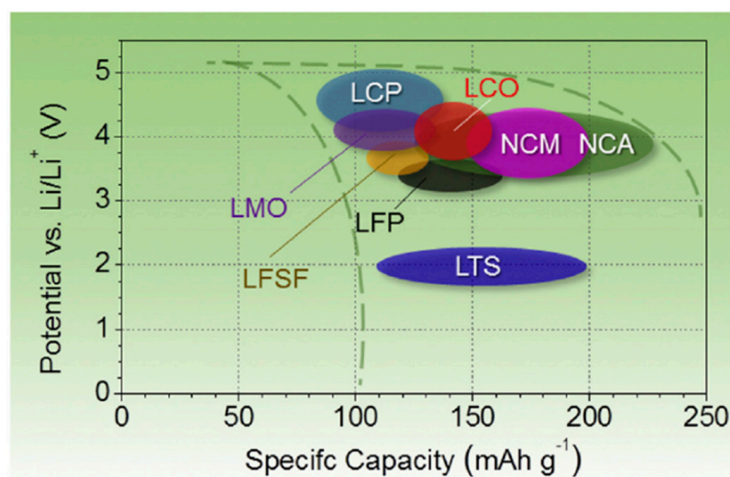


Figure 1. Theoretical capacity of lithium-ion battery (LIB) cathode material by type [4].

Table 1. Comparison of characteristics of cathode active material for a lithium secondary battery (Source by SNE Research) [2].

	LCO	NCM	NCA	LMO	LFP
Structure	Layered	Layered	Layered	Spinel	Olivine
Specific (mAh/g)	272	272	160	148	170
Operating Voltage (V)	3.7	3.6	3.6	4	3.2
Stability	Good	Rather Good	Poor	Good	Very Good
Cycle Life	Good	Medium	Good	Poor	Good
Application	Small	Small, Medium, and Large	Medium	Medium and Large	Medium and Large

However, problems such as structural instability (LNO), performance degradation at high temperatures (LMO), and low ion conductivity (LFP) lead to inferior performance characteristics in comparison with commercialized LCO materials. These problems have led to the development of $\text{LiNi}_{1-x-y}\text{Co}_x\text{Mn}_y\text{O}_2$ (NCM) materials which combine the advantages of LNO's high capacity, LMO's excellent thermal stability and low cost, and LCO's stable electrochemical characteristics. NCM is characterized by high capacity, excellent lifetime characteristics and stability and is used in various applications such as ESS for electric appliances, electric vehicles, and electric power systems. The discharge capacity and the potential for determining the energy density of the active material vary greatly depending on the structure of the material and the type of dislocation metal. In order to design an optimum BMS, it is necessary to know the characteristics of each material.

2.1. Spinel Structure Compound (LiMn_2O_4)

LiMn_2O_4 , which has a spinel structure, is somewhat lower in capacity (120–130 mAh/g) than LCO, a commercial cathode material, but its operating voltage is much higher, and its material cost is much lower than Co. It is thus a material that is suitable for large lithium-ion batteries such as those used in electric vehicles and renewable energy storage systems [1,2]. The current research trend is concentrated on improving both its safety and electrochemical properties by mixing spinel LMO with other layered compounds.

As shown in Figure 2, because the spinel structure is a 3D structure, the migration path of Li-ions is short and the ion conductivity is high, so it lends itself advantageously to a high charging and discharging rate. It is also thermally stable even in the charging state. When an over-discharged state is reached, however, the Li content diffuses into the inside of the structure. This destroys the thermal equilibrium and irreversible phase transition occurs from the cubic system (a , b , and c of the unit lattice are same, and the axial angle α , β , γ is 90°) to the tetragonal system (a structure having two vertical axes orthogonal to the left and right and a vertical axis perpendicular to the horizontal axis) [2].

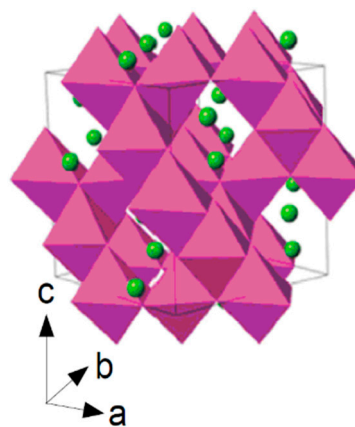


Figure 2. Crystal structure of the three lithium-insertion compounds in which the Li^+ ions are mobile through the 3D (spinel) framework [3].

Therefore, LMO is used only in the 4 V region and has an actual capacity of approximately 120 mAh/g [2–4]. The Mn^{3+} in the LMO mainly causes Jahn–Teller distortion (the structure of the cathode material distorts at the time of charging and discharging of the lithium-ion battery), which causes performance degradation at room temperature. It is possible to improve the lifetime characteristics at room temperature by keeping the average oxidation number of Mn at 3.5 or more [2].

2.2. Olivine Compound ($LiFePO_4$)

Figure 3 shows the olivine crystal structure of $LiFePO_4$. $LiFePO_4$ has a very stable structure due to the presence of strong P–O bonding forces, unlike the layered positive electrode material. It also has excellent stability compared with other positive layered electrode materials. However, poor Li-ion conductivity is a major disadvantage of LFP. This is because the volume for migration of Li-ions is relatively small due to the strong binding forces, and thus charging and discharging are only possible at very low current densities at room temperature.

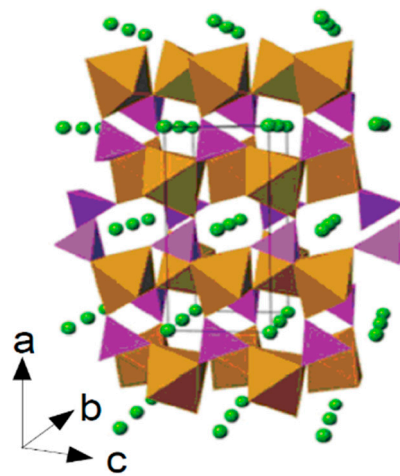


Figure 3. Crystal structure of the three lithium-insertion compounds in which the Li^+ ions are mobile through the 1D (olivine) framework [3].

However, since it can realize an actual capacity (160–170 mAh/g) of close to 100% of its theoretical capacity and has excellent lifetime characteristics, it has attracted attention as a cathode material for a lithium-ion secondary battery [2–4].

2.3. Layered Compound

Since 2005, the ternary layered structure material Ni–Co–Mn has been applied as a cathode material. As cobalt costs have surged, the layered structure material has been applied as a substitute for lithium cobalt oxide (according to SNE Research, LCO and NCM-based materials accounted for more than 60% of the global cathode market in 2016) [2].

As shown in Figure 4, the layered compound has a structure in which Li, a transition metal, and oxygen have a regular arrangement. Li-ion intercalation-deintercalation is possible between the transition metal and the metal oxide layer containing bound oxygen molecules. Ion conductivity is high because it diffuses along the two-dimensional plane.

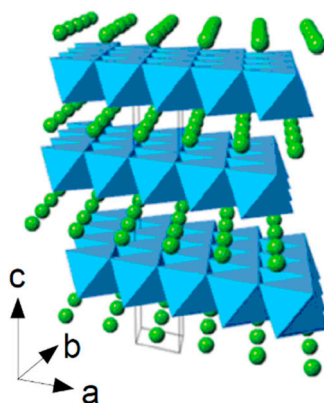


Figure 4. Crystal structure of the three lithium-insertion compounds in which the Li⁺ ions are mobile through the 2D (layered) framework [3].

2.3.1. LiCoO₂

LiCoO₂ (LCO) material, which was originally used by Sony in 1991 for the mass production of LIB, is widely used because it is easy to manufacture and easy to mass-produce. It accounts for 30–40% of the cathode material usage even though it makes use of expensive raw materials. LCO is characterized by a high operating potential; however, when the amount of lithium to be desorbed increases due to charging and discharging, a problem arises due to a phase change. In this state, the structure becomes unstable, the Co ions are eluted, and an oxidation/reduction reaction of the electrolyte may occur. Therefore, in order to realize its use in a battery, the amount of lithium to be desorbed should be limited from 0 to 0.5 (0~50%). As a result, the actual capacity is lowered to approximately 120 to 130 mAh/g in comparison with the theoretical capacity of 272 mAh/g [2–4]. LCO forms two structures depending on the heat treatment temperature used in manufacture. The synthesis method used is known as the solid-phase reaction method. This method involves mixing powders containing elements, such as oxides, and reacting the mixture at high temperatures. When synthesized at 800 °C or higher, a layered LCO is formed. A spinel structure is formed at approximately 400 °C [6]. However, since the electrochemical characteristics of the structure synthesized at a lower temperature degrade due to internal defects and low crystallinity, the high temperature layered LCO is mainly used as the cathode active material [7].

2.3.2. LiNiO₂

LiNiO₂ (LNO) is a material that can increase the reversible capacity when compared with LCO because lithium can be desorbed from 0 to 0.7 (0~70%). It is considered a substitute for LCO because it is cheaper than Co and stable in terms of supply. However, as Ni²⁺ is stable compared to Ni³⁺, some Ni²⁺ occupy Ni³⁺ sites and some Li-ion sites. It is thus very difficult to synthesize compared to LCO.

LNO is not a promising material for commercial lithium-ion cells. However, mixed LiNi_{1-y}Co_yO₂ phases can overcome the main drawbacks exhibited by both LCO and LNO oxides [8–10]. For example, the solid solutions LiNi_{0.85}Co_{0.15}O₂ and LiNi_{0.80}Co_{0.15}Al_{0.05}O₂ have been shown to exhibit attractive electrochemical properties with a reversible capacity of ~180 mAhg⁻¹ and excellent cyclability [11].

2.3.3. LiNi_{1-x-y}Co_xMn_yO₂

LiNi_{1-x-y}Co_xMn_yO₂ (NCM) material combines advantages such as the high capacity of LNO, the excellent thermal stability and low cost of LMO, and the stable electrochemical properties of LCO. As the Ni content increases, the capacity increases. As the amount of Co increases, the output power increases. As the Mn content increases, the stability increases. It is also economical. Figure 5 shows these features. Unlike LCO, irreversible phase transition is low even when the amount of lithium to be desorbed is large, allowing a high capacity to be realized along with excellent lifetime characteristics.

Due to these characteristics, it is attracting attention as a primary material that is appropriate for use in mainstream applications, such as ESS or electric vehicle (EV) systems.

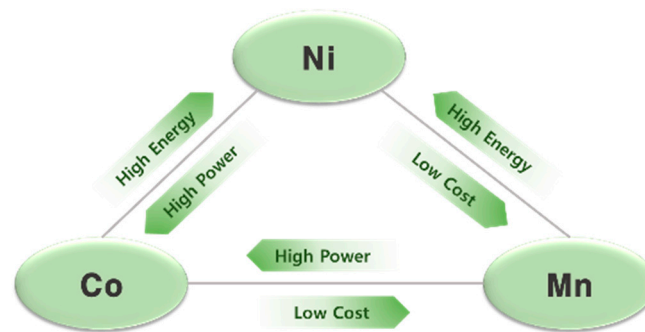


Figure 5. Transition metal characteristics of NCM LIB.

However, since the ion radii of Ni^{2+} (0.69 \AA) and of Li^+ (0.76 \AA) are similar, cation-mixing (in which Ni and Li change their positions and form crystal structures) occurs frequently when the Ni content increases [12–18]. As a result, the performance and life of the battery deteriorates. Accordingly, recent research trends are concentrated on improving stability while increasing the Ni content.

3. Comparison of Properties According to Ni Content

3.1. Performance Evaluation Experiment

A performance and life test were carried out to compare and analyze the characteristics of LIBs with varying Ni contents. Experiments were performed using the equipment and batteries shown in Figure 6. The experimental test equipment used was the MACCOR series4000 test system (MACCOR, Tulsa, OK, USA). The battery arrangement used was a pouch-type 20 Ah-scale full cell. Two batteries were used in the experiment. The NCM523 battery had a Ni:Co:Mn composition ratio of 5:2:3, and the NCM622 battery had a Ni:Co:Mn composition ratio of 6:2:2.

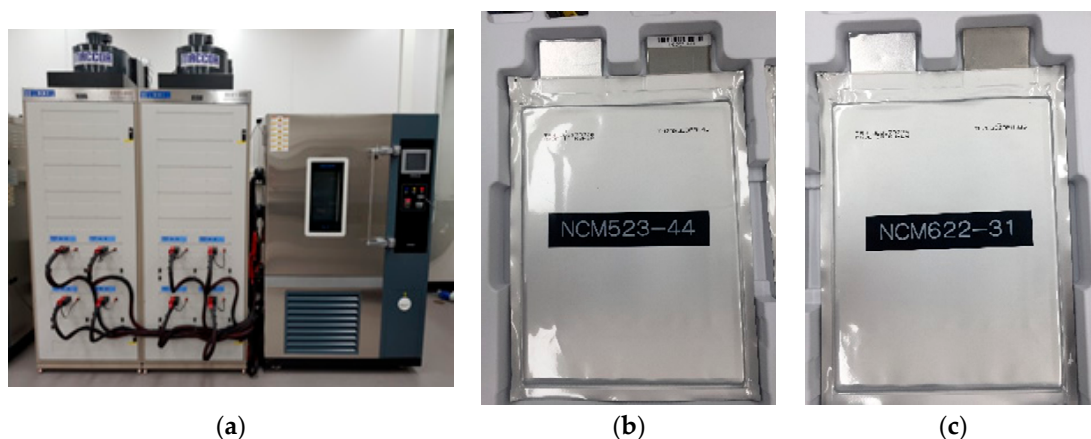


Figure 6. Experimental equipment. (a) Charger-Discharger [series4000, MACCOR] (b) Pouch Type 20 Ah-scale NCM523 battery. (c) Pouch Type 20 Ah-scale NCM622 battery.

3.1.1. C-Rate Charging/Discharging Test

As a basic performance evaluation, a charge-discharge test was performed for each C-rate. For the C-rate charging test, the C-rate charging current was changed in the following sequence: 0.5, 1, 2, 3, 4, 5. The dynamic characteristics of the battery were analyzed for each C-rate. For the C-rate charging test, the discharging C-rate was set to 0.5, and only the influence on the charging current was considered. For the C-rate discharging test, the discharging current C-rate was changed in the following sequence:

0.5, 1, 2, 3, 4, 5. Moreover, only the effect on the discharge current was considered. The charging test procedure followed in the study was as follows: charging (0.5, 1, 2, 3, 4, 5 C-rate), rest 30 min, discharging (0.5 C-rate), and rest 30 min. In order to analyze the performance characteristics of the battery at varying temperatures, from low to high, a temperature chamber was used, and experiments were conducted at temperatures of 10, 15, 25, 30, 40, and 60 °C.

In the case of the charge test, the battery was charged using the Constant Current/Constant Voltage (CC/CV) method for the full charge. The termination condition at CV was taken as the moment when the current reached 1/20 of the rated capacity. Figure 7a,b show the C-rate charge test and Figure 7c,d show the C-rate discharge test. It can be seen that with a higher C-rate, the time to reach the set upper limit voltage of 4.2 V was reduced, but the CV section increased. With a lower C-rate, the battery capacity remained high.

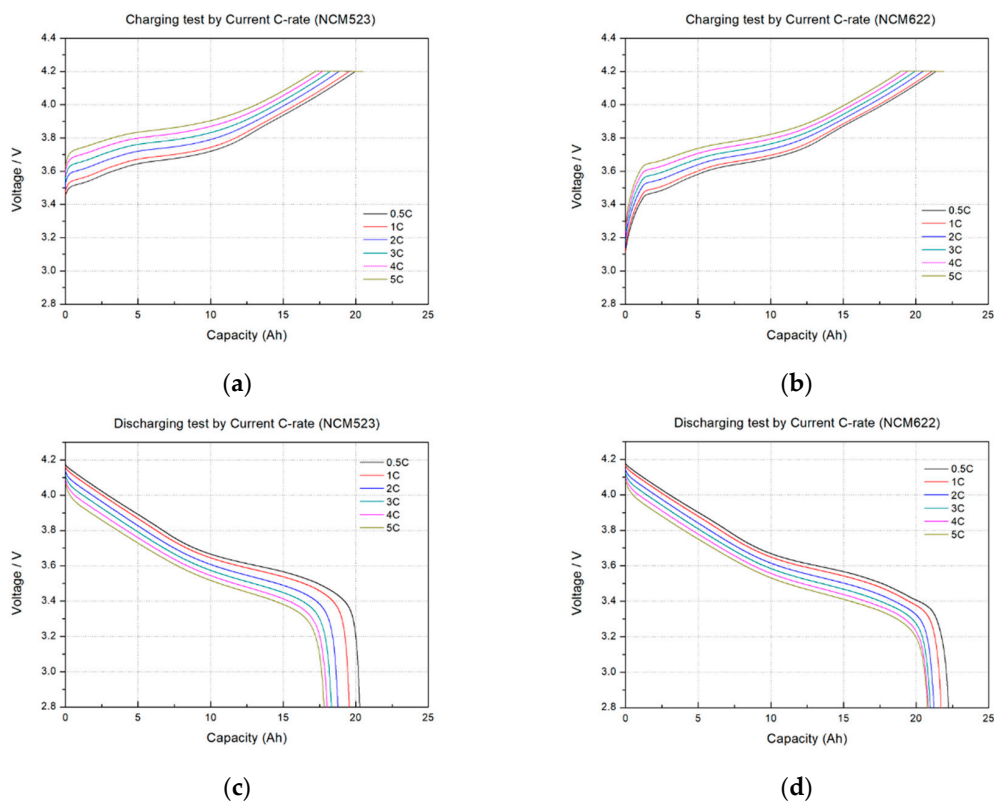


Figure 7. Charging-discharging test at specific current C-rates [0.5 1 2 3 4 5]. (a) NCM523 (charging test) (b) NCM622 (charging test). (c) NCM523 (discharging test) (d) NCM622 (discharging test).

The NCM523 and NCM622 demonstrated capacities close to 20 Ah in the region of 0.5 to 5 C-rate, but the NCM622 with high Ni content demonstrated higher capacity than that of the NCM523. The NCM523 demonstrated a capacity of 20 Ah or more at a low C-rate of 0.5 C, but the NCM622 demonstrated a capacity of 20 Ah or more in all C-rate regions.

Figure 8 shows the charge-discharge efficiency of the NCM523 and NCM622. A high efficiency of 90% or more was observed at 10–60 °C with higher efficiency when the test was performed at low C-rates. In the case of the NCM523 charge test, the efficiency was 96–98% (10–60 °C) at the low C-rate of 0.5 C and 91–96% (10–60 °C) at the high C-rate of 5 C. In the discharge test, the efficiency was 91–96% (10–60 °C) at 0.5 C and 89–94% (10–60 °C) at 5 C. The efficiency of the NCM622 was 97–99% at 0.5 C and 92–96% at 5 C. In the discharge test, the efficiency was 94–99% at 0.5 C and 92–97% at 5 C. As the charge current increased, the efficiency decreased over all experimental temperature ranges. Because overvoltage occurs with high current, the discharge energy decreases due to the degradation of the insertion/desorption of Li-ions because of the increase in the reaction rate.

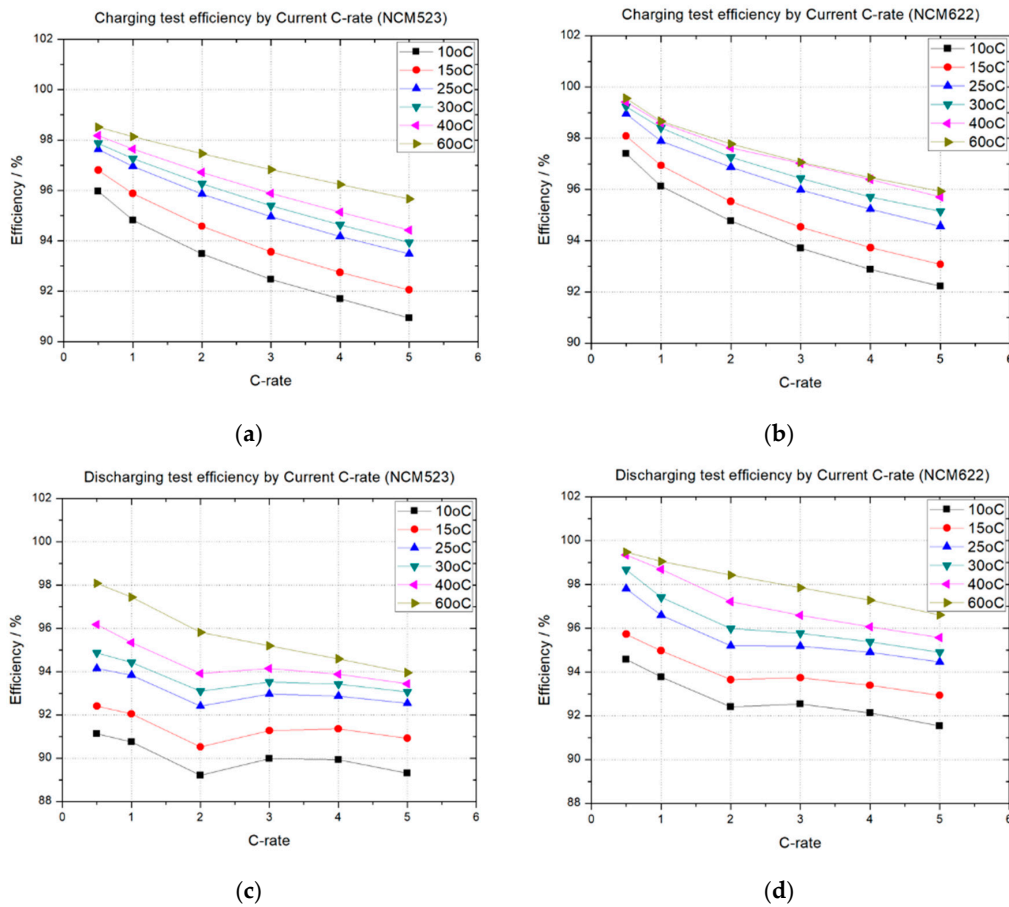


Figure 8. Charging–discharging efficiency at specific temperatures (10 °C 15 °C 25 °C 30 °C 40 °C 60 °C). (a) NCM523 (charging test) (b) NCM622 (charging test). (c) NCM523 (discharging test) (d) NCM622 (discharging test).

At all experimental temperatures and C-rates, the NCM622 demonstrated higher efficiency than the NCM523 and showed more of a difference in the discharging test than in the charging test. This demonstrated that the NCM622 is a more efficient battery than the NCM523 for applications requiring high output and operation at various temperature ranges.

3.1.2. Hybrid Pulse Power Characterization (HPPC)

A hybrid pulse power characterization (HPPC) test was performed at various test temperatures (10, 15, 25, 30, 40, and 60 °C) and state of charge (SOC) percentages (10–90%). Figure 9 shows the evaluation pattern for the HPPC experiment. The HPPC test method was used to apply a 10 s discharge pulse of 100 A (5 C-rate) and then a 10 s charge pulse of 75A (3.75 C-rate). There was a rest time of 40 s between discharge and charge to stabilize the battery voltage. This test was implemented to measure the maximum charge-discharge output power and resistance of the battery using the voltage change in the current. It is a useful performance evaluation test since it provides the output power and resistance characteristics of each cell in accordance with a change in the SOC. Output power and resistance can be calculated using the following Equations (1)–(4) by utilizing the voltage and current data obtained from the test [19–21]:

$$R_{\text{chg}} = \Delta V / I = (V_{\text{chg}} - \text{OCV}_{\text{chg}}) / I_{\text{chg}} \tag{1}$$

$$R_{\text{dis}} = \Delta V / I = (\text{OCV}_{\text{dis}} - V_{\text{dis}}) / I_{\text{dis}} \tag{2}$$

$$\text{Charge pulse power} = V_{\text{MAX}} \times I_{\text{MIN}} = V_{\text{MAX}} \times (V_{\text{MAX}} - \text{OCV}_{\text{chg}}) / R_{\text{chg}} \tag{3}$$

$$\text{Discharge pulse power} = V_{\text{MIN}} \times I_{\text{MAX}} = V_{\text{MIN}} \times (\text{OCV}_{\text{dis}} - V_{\text{MIN}}) / R_{\text{dis}}. \tag{4}$$

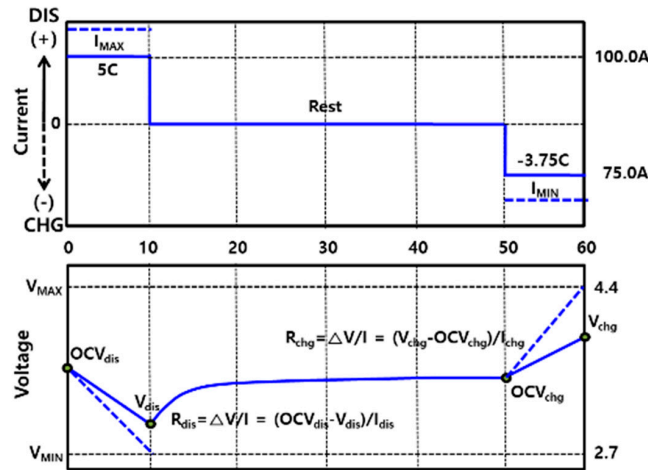


Figure 9. Hybrid power pulse characteristics evaluation pattern.

Figure 10 shows the output power and resistance of the NCM523 and NCM622 batteries, calculated from the experiment. As the temperature increased, the output characteristics improved and the resistance tended to decrease. The nominal energy of the NCM523 and NCM622 was 73 Wh. The charging output power range of the NCM523 at 10 °C in comparison with the nominal energy lies between C-rates of 6.2 (449.3 W) and 12.4 (908.8 W), and the discharging output power range lies between C-rates of 3.1 (229.9 W), and 16.4 (1200.8 W). In the case of the NCM622, the charging output power range lies between C-rates of 6.6 (483.2 W) and 14.5 (1064.6 W) at 10 °C and the discharge output power range lies between 7.6 (557.2 W) and 17.5 (1276.6 W). The charging output power range of the NCM523 at 60 °C lies between C-rates of 13.9 (1012.9 W) and 34.5 (2519.2 W) and the discharging output power range lies between C-rates of 24.6 (179.9 W) and 38.3 (2798.5 W). The charging output power range of the NCM622 at 60 °C lies between 16.2 (1181.9 W) and 42.0 (3067.9 W) and the discharging output power range lies between C-rates of 29.4 (2148.3 W) and 44.1 (3218.4 W).

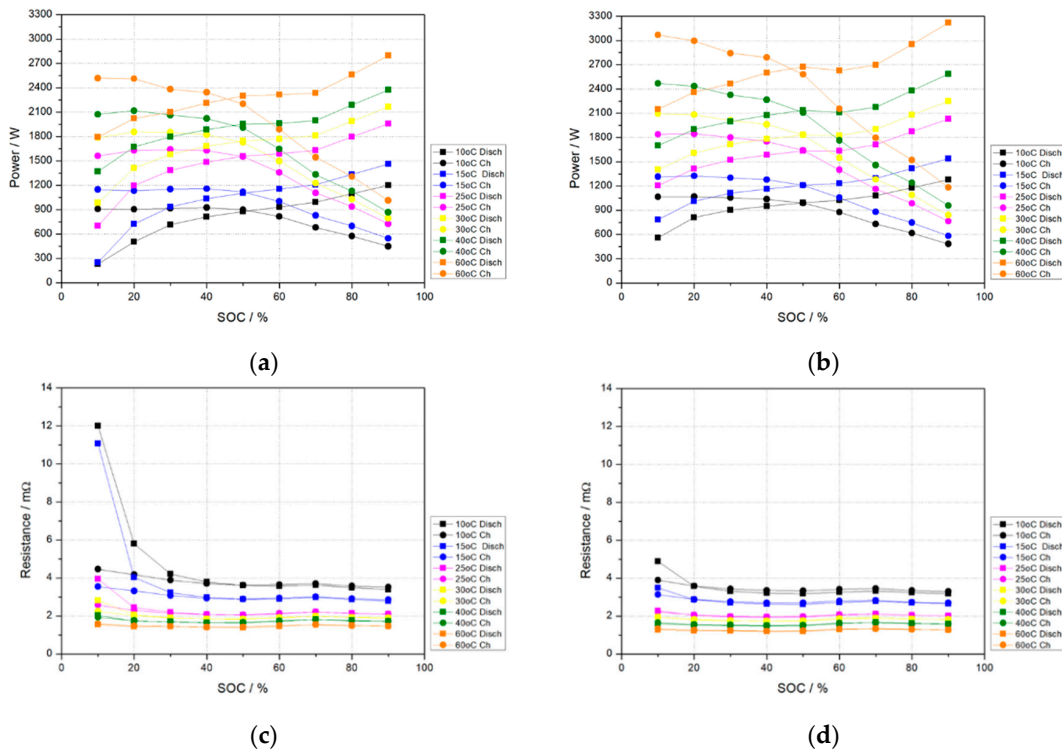


Figure 10. HPPC experiment (10, 15, 25, 30, 40, and 60 °C). (a) NCM523 HPPC power, (b) NCM622 HPPC power, (c) NCM523 HPPC resistance, (d) NCM622 HPPC resistance.

Compared with the NCM523, the NCM622 has excellent output characteristics and low resistance at all test temperatures and in all SOC regions. In particular, at the low temperatures of 10 and 15 °C, the resistance of the NCM523 increases significantly, which leads to decreases in the output characteristics. Therefore, when the required output power is greater than 4 C, the output power of the NCM523 may not meet the required output power. Control strategies that do not take into account the temperature characteristics of the battery and the state of charge may lead to excessive use of the battery, which has a direct effect on the life of the battery. Therefore, it is essential to establish a control strategy that considers the various characteristics of each type of battery for optimal ESS operation.

3.2. Comparison of Life Performance (NCM523 vs. NCM622)

Accelerated deterioration experiments involving charging and discharging at 4 C-rate current were conducted to analyze the lifetime characteristics of NCM523 and NCM622. As the cycle proceeded, a comparison of lifetime characteristics and a dQ/dV (differential capacity) analysis of the NCM523 and the NCM622 were conducted.

3.2.1. Accelerated Deterioration Experiment

Figure 11 shows the charge-discharge profile used in the accelerated deterioration test. The test current was set at 80 A, which is the 4 C-rate current of the 20 Ah scale battery. The test was performed from 2.8 V (cut-off voltage) to 4.2 V (upper limit voltage). A 30-min rest time was provided between charge and discharge to stabilize the battery.

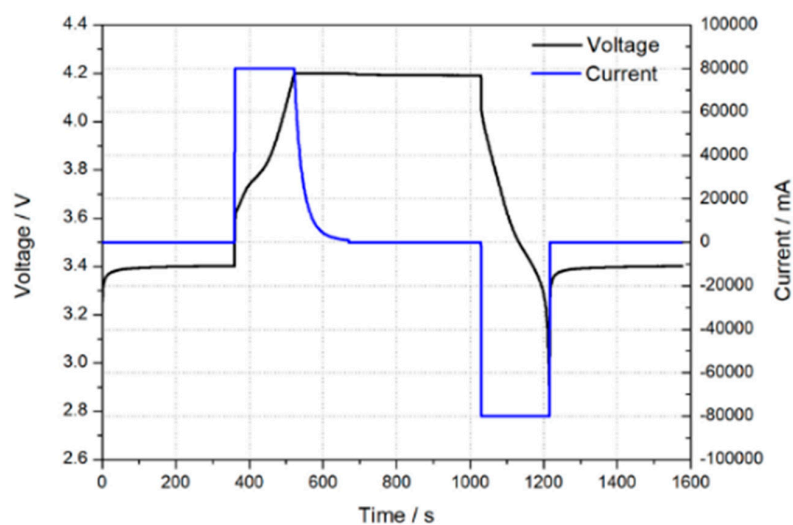


Figure 11. Cycle test profile, voltage vs. current (4 C current).

Figure 12 shows the cycle lifetime characteristics of the NCM523 and the NCM622 at 25 and 30 °C, respectively. In many applications, a battery is considered to have reached the end of its life when the battery capacity reaches 80% of the initial capacity. For experiments conducted at 25 °C, the NCM523 reached 80% of the initial capacity at 3370 cycles, and the NCM622 reached 80% at 1070 cycles. At 30 °C, the NCM523 reached 80% at 2649 cycles, and the NCM622 reached 80% at 741 cycles. Because battery design and manufacturing technology varies with every battery manufacturer, these results may differ, but Figure 12 shows that the cycle life of the NCM523 is significantly superior to that of the NCM622.

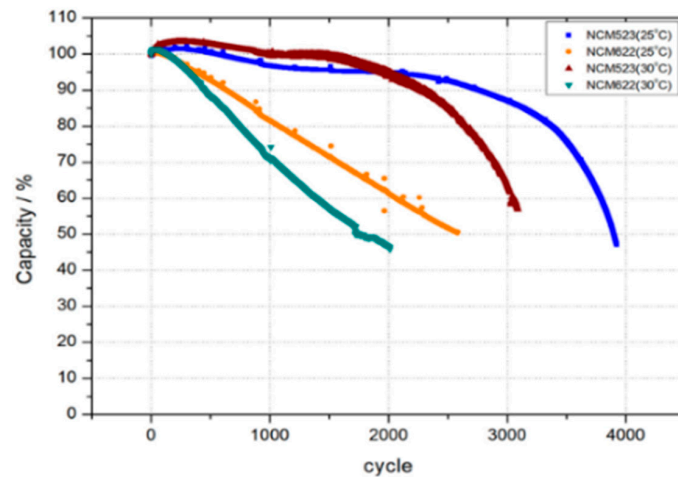


Figure 12. Cycle life test (25 °C vs. 30 °C).

As can be seen from the performance analysis, performance characteristics such as the output power characteristics and the efficiency were improved when the temperature rose. However, when the temperature increased from 25 to 30 °C, the cycle lifetime (to 80% of the initial battery capacity) of the NCM523 decreased by approximately 700 cycles compared to its performance at 25 °C. The cycle lifetime of the NCM622 decreased by approximately 300 cycles compared to its performance at 25 °C. Compared with the NCM622, the NCM523 showed a significant improvement in lifetime characteristics because the NCM523 has a high Mn ratio, which improves battery stability. Because the Ni content of the NCM622 is higher than that of the NCM523 (which makes the cation-mixing of the NCM622 occur more easily compared to the NCM523), the cation-mixing reduces the lifetime characteristics of the NCM622. Figure 13 shows the surface states of the NCM523 and the NCM622 after the accelerated deterioration experiment at 25 °C. After 3900 cycles, the life of the NCM523 was degraded to approximately 45% of its initial capacity. The NCM622 was degraded to approximately 50% of its initial capacity after 2700 cycles.

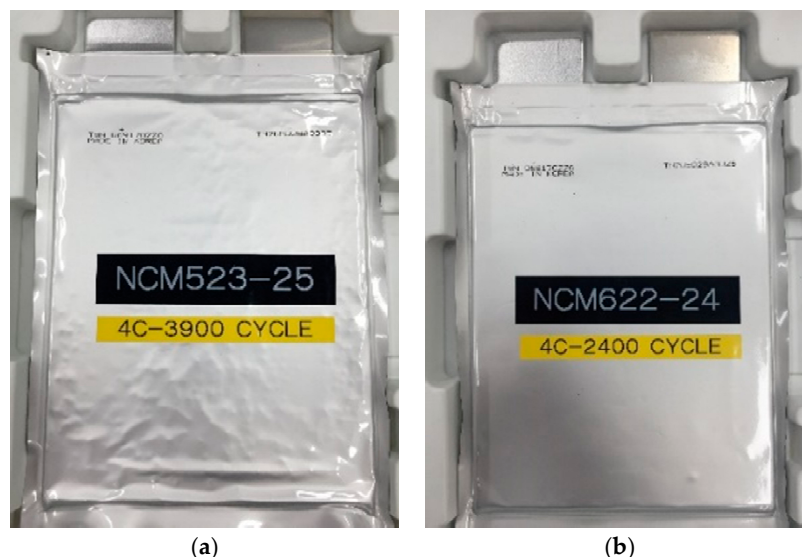


Figure 13. Change in battery appearance after accelerated deterioration experiment. (a) NCM523 (After 3900 cycle at 80 A); (b) NCM622 (After 2400 cycle at 80 A).

3.2.2. dQ/dv

Figure 14 shows the dQ/dv graph of the NCM523 and NCM622 measured during the accelerated deterioration test. As the deterioration of the battery progressed, it was possible to see the dynamic

characteristics of the capacity versus the changing voltage. This indicated a deformation of the internal structure of battery [3,15,22].

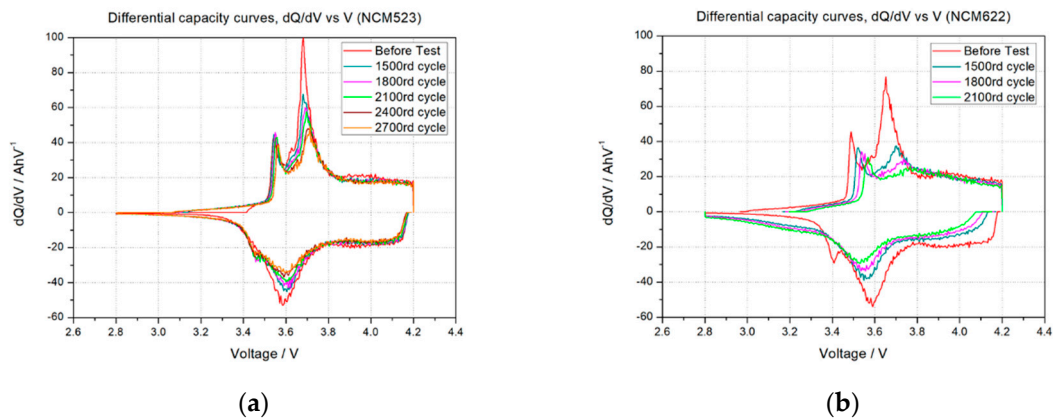


Figure 14. Differential capacity curves. (a) NCM523 (1500, 1800, 2100, 2400, and 2700 rd cycle). (b) NCM622 (1500, 1800, and 2100 rd cycle).

The peak position of the NCM523 is at 3.5–3.6 V (small peak) and 3.7 V (large peak) when charging, and at 3.6 V when discharging. As the deterioration progresses, the position of the peak does not change much but the size of the peak decreases. In the case of the NCM622, a peak is formed in the vicinity of 3.5 V (small peak) and at 3.65 V (large peak) (similar to the NCM523 at the beginning of the experiment), and a peak is formed at 3.6 V when discharging. However, as the deterioration progresses, the peak shifts to a higher potential when charging and to a lower potential when discharging. Of course, the size of the potential peak decreases as the deterioration progresses.

3.3. Electrochemical Impedance Spectroscopy (EIS) and Battery Parameters

EIS experiments were conducted using the equipment shown in Figure 15a. EIS is a method of measuring the impedance using the response characteristics of the battery when a sinusoidal voltage or current signal is provided to the battery. As shown in Figure 15b, the impedance is measured from high frequency to low frequency. At high frequency, the series resistance (R_s) of the battery is measured, and the charge transfer resistance (R_c) is measured at the mid-frequency. At low frequencies, the diffusion resistance (R_d) (which occurs as ions move) is measured [23–25].

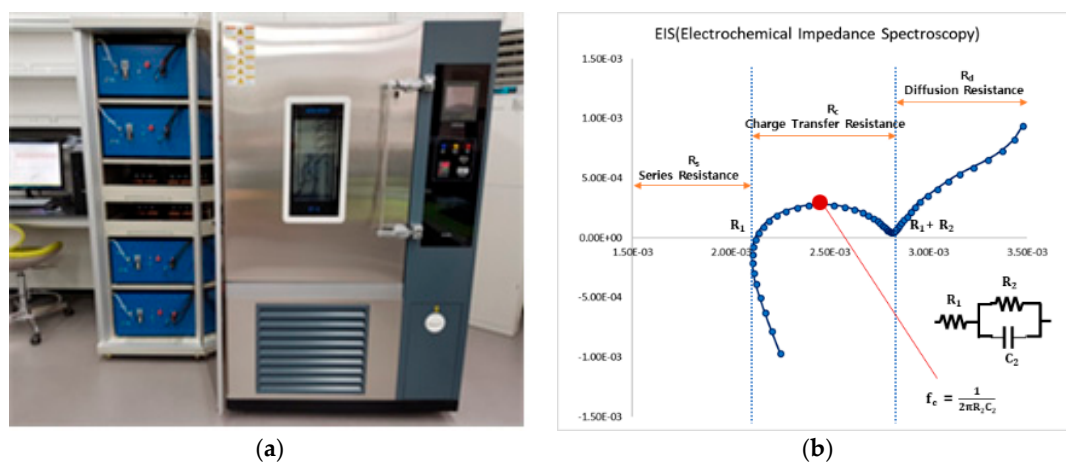


Figure 15. Electrochemical impedance spectroscopy (EIS). (a) Instrument for EIS test [HCP-1005, BioLogic]; (b) EIS and equivalent circuit.

Figure 16 shows the results of the EIS experiments with the SOC changing in 5% decrements from 100% to 0% at 25 °C using the NCM523 and NCM622 batteries. In the case of R_s , which is an index of

deterioration, there was no significant change when the SOC was changed. R_c demonstrated different results as SOC changed. The R_c was affected more by the anode than the cathode, and the value of R_c decreased as the SOC increased. It is believed that as the charging progressed, reduction reactions occurred between the lithium-ions and the graphite of the negative electrode which increased the conductivity of the negative electrode, thereby lowering the resistance.

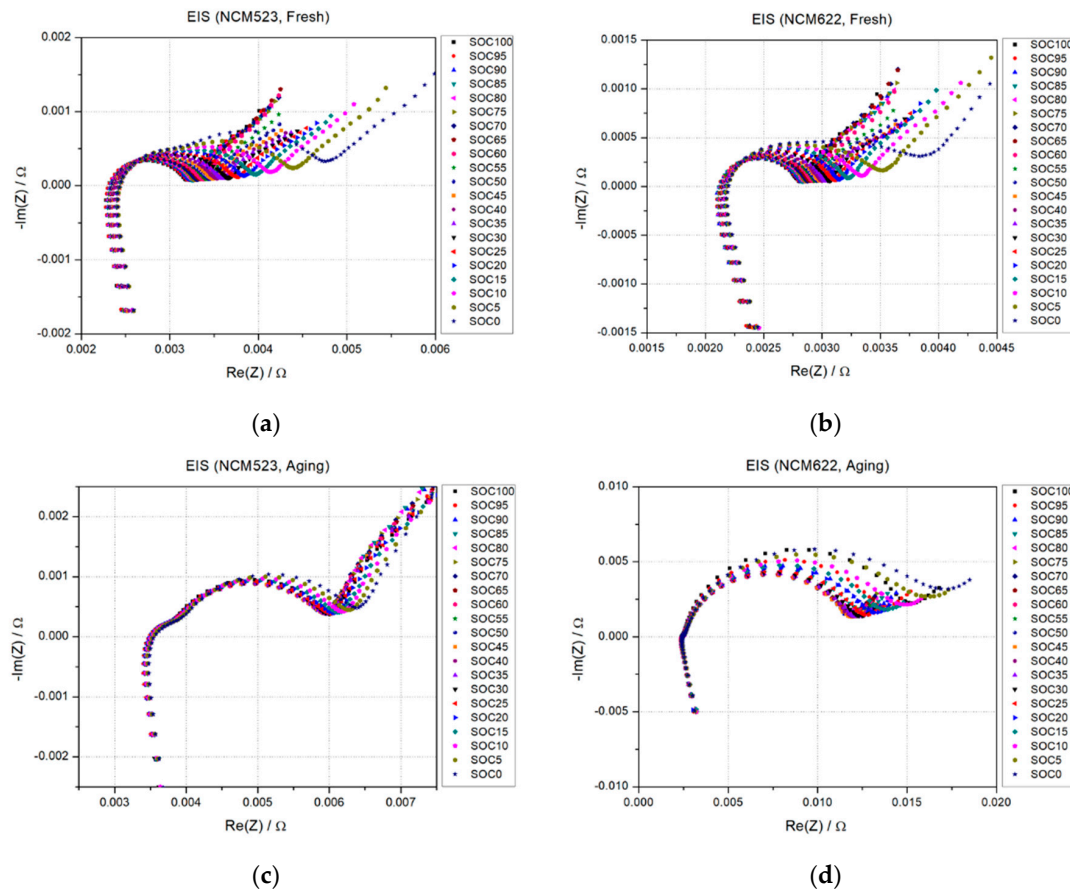


Figure 16. Electrochemical impedance spectroscopy at specific state of charge (SOC) values. (a) Fresh NCM523. (b) Fresh NCM622. (c) Aging NCM523 (After 3900 cycle at 80 A). (d) Aging NCM622 (After 2400 cycle at 80 A).

Figure 17 shows the magnitude change of the charge transfer resistance of the fresh and aging states of the NCM523 and NCM622 as the SOC deteriorated. Before the deterioration test, the R_c of NCM523 and NCM622 showed only a small difference in the order of several $\text{m}\Omega$, but the NCM622 showed a large increase in R_c compared to the NCM523 after deterioration.

Since conductivity increased at high SOC before deterioration, the resistance of the battery decreased with an increase in SOC. However, as deterioration progressed, Figure 17 shows that the resistance of the battery increased from 60% SOC to higher SOC values. When a battery is used, a solid electrolyte interphase (SEI) layer is formed on the anode. It serves as a kind of protective film because it prevents side reactions between lithium-ions and other materials during charging-discharging cycles. However, as the SEI layer increases in thickness, the interfacial resistance increases, which causes the battery temperature to rise and leads to deterioration.

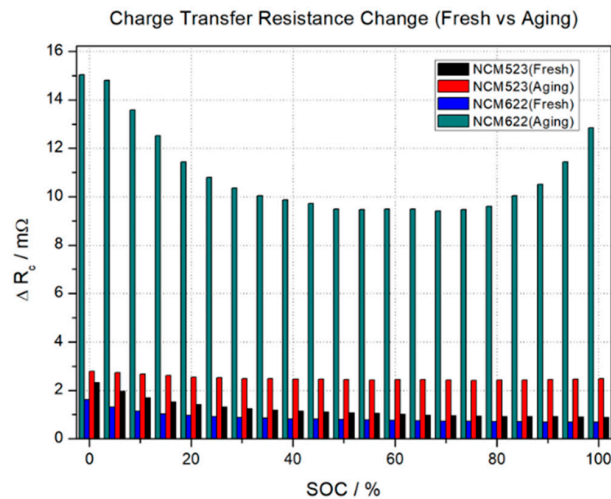


Figure 17. Change of charge transfer resistance (fresh vs. aging).

When a sinusoidal voltage is applied to the battery in an EIS test, the voltage, current, and impedance can be expressed as follows:

$$V(t) = \bar{V} + \hat{V} \sin(\omega t) \tag{5}$$

$$I(t) = \bar{I} + \hat{I} \sin(\omega t + \phi) \tag{6}$$

$$Z(j\omega) = \frac{V(j\omega)}{I(j\omega)} = \frac{\bar{V}}{\bar{I}} e^{-j\phi} = |Z| e^{j \cdot \text{Arg}(Z)} = \text{Re}(Z) + j \cdot \text{Im}(Z). \tag{7}$$

\hat{V} and \hat{I} are the voltage and the current amplitude, respectively; \bar{V} and \bar{I} are the voltage and the current (DC) values; f is the test signal frequency; $\omega = 2\pi f$ the angular frequency; and ϕ is the phase difference between $V(t)$ and $I(t)$. $V(j\omega)$ and $I(j\omega)$ the Steinmetz transforms of $V(t)$ and $I(t)$ [23]. The battery equivalent circuit of the EIS, as shown in Figure 15b, can be constructed with the impedance and the parameters R_1 , R_2 , and C_2 of the battery equivalent circuit, which can be estimated using the following Equations (8) and (9).

$$Z(f) = R_1 + \frac{R_2}{1 + i2\pi f R_2 C_2} \tag{8}$$

$$f_c = \frac{1}{2\pi R_2 C_2}. \tag{9}$$

The parameters estimated from the AC impedance were compared to the parameters of the DC impedance implemented in the ECM model.

3.4. ECM Model and Battery Parameters

The equivalent circuit model (ECM) simply expresses the series resistance (R_1) of a battery along with the dynamic characteristics generated by the time constant as RC (R_2 , C_2), and estimates these parameters based on the battery’s response to a given input [26–30]. When combined with multiple electrical filters and artificial intelligence algorithms for battery performance and life prediction, the accuracy of the ECM can be increased. The RC ladder connected to R_1 can be added to as much as necessary, but it is important to set an appropriate number for the ladder because it directly affects the computational speed of the algorithms. The parameters are estimated as a configuration that has R_1 and an R-C ladder in series.

Figure 18 shows the dynamic characteristics of the voltage when a discharge current pulse is provided in one SOC interval. R_1 , which can be estimated by instantaneous IR droop, can be calculated simply by using Equation (10), and R_2 and C_2 can be estimated by considering the time constant. Here,

the time constant is defined as the time when the voltage decreases to 63.2% of the normal voltage. R_2 and C_2 are calculated using Equations (11) and (12):

$$R_1 = \frac{\Delta V_1}{\Delta i} \tag{10}$$

$$\tau = R_2 \cdot C_2 \tag{11}$$

$$R_2 = \left| \frac{\Delta V_2}{\Delta i} \right| - R_1. \tag{12}$$

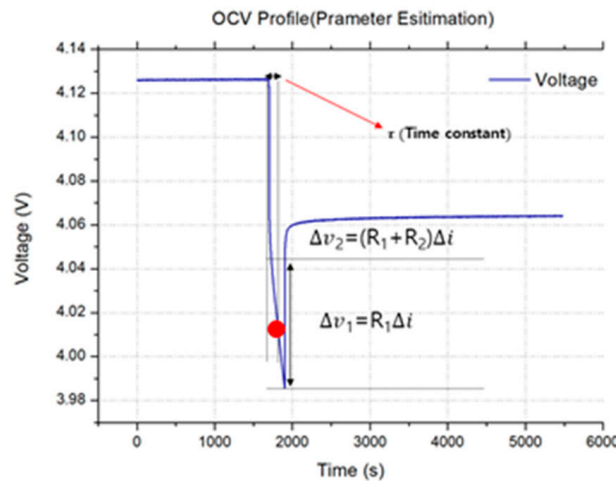


Figure 18. One pulse from the discharge test.

Figure 19 shows the AC impedance parameters estimated using Equations (8) and (9) for the EIS measurement data. In the case of NCM523, the R_1 value tended to decrease when the temperature rose, but NCM622 showed a sharp increase in resistance at 40 °C. This characteristic of NCM622 can be confirmed with the DC method as well. Because the Mn content of NCM622 is relatively low compared to NCM523, it is presumed to demonstrate instability at high temperatures. For the R_2 value, both the AC and DC methods showed a tendency to increase with decreasing temperature. In the case of C_2 , the value of the parameter rose as the temperature increased, and it could be seen that it changed unstably with varying SOC values.

It can be confirmed that the characteristic trajectory of the overall impedance is similar, although the scale of the parameter values of the AC method and the DC method are different. Through analysis of AC·DC parameter characteristics, NCM LIB showed poor impedance characteristics at low temperatures, and R_2 increased rapidly at low SOC values. It is clear that NCM batteries should not be operated at low temperatures or in a low SOC in order to improve battery performance and lifetime.

Figure 20 shows the results of battery modeling using the AC impedance and DC impedance parameters of NCM523 and NCM622, which were estimated in the temperature range of 10 to 40 °C. To verify the modeling results, the SOC was calculated using Equation (13), and the battery voltage was calculated by applying the estimated parameters corresponding to the current SOC to Equations (14) and (15). The initial SOC of the model was set at 100%, and the Q , indicating the battery capacity, was input based on the discharge capacity measured before the experiment was conducted [26].

$$SOC(t + 1) = SOC(t) - \frac{\Delta t}{Q} \eta(t) \cdot i(t) \tag{13}$$

$$iR_2(t + 1) = \exp\left(-\frac{\Delta t}{R_2 C_2}\right) \cdot iR_2(t) + (1 - \exp\left(-\frac{\Delta t}{R_2 C_2}\right)) \cdot i(t) \tag{14}$$

$$V(t) = OCV(SOC[t]) - R_2 \cdot iR_2[t] - R_1 \cdot i[t]. \tag{15}$$

Figure 20 shows that the overall modeling results were similar to the experimental data. Before performing experiments for estimating parameters for various SOC at 10, 25, and 40 °C, the real capacity (to be applied to the model) was obtained through a capacity measurement test in which the battery was discharged from a fully charged state to 2.8 V at a 1 C-rate current (nominal capacity: 20 Ah). By applying this, the model was able to estimate the SOC accurately, and the modeling accuracy was further improved by applying the parameters at various SOC values. As shown in Figure 21, the voltage error (between the experimental results and the model) for NCM622 was larger than that for NCM522. The voltage error was also larger at low SOC values. The voltage error for NCM523 and NCM622 increased with a decreasing temperature and decreased with an increasing temperature.

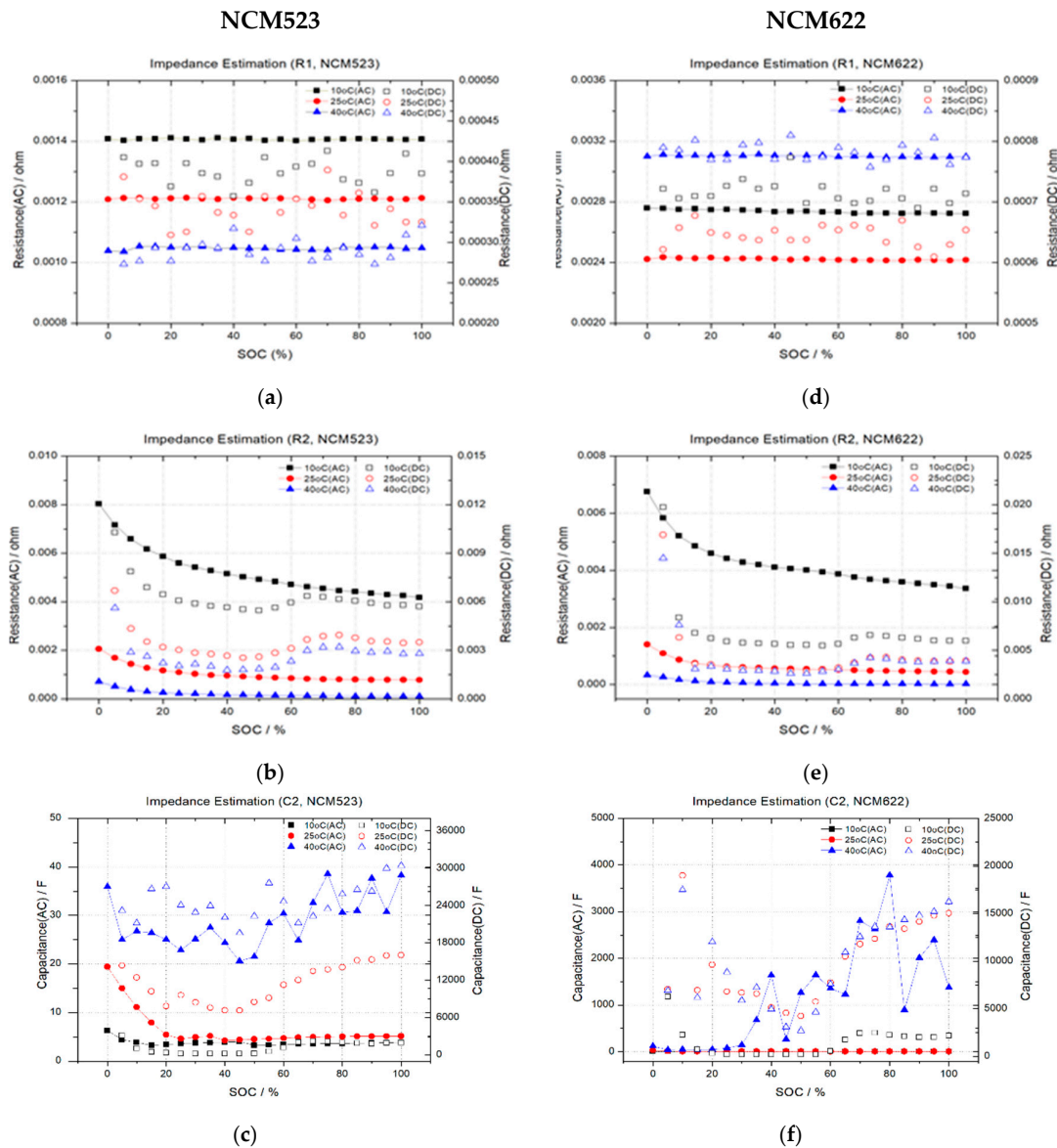


Figure 19. Battery parameter estimation by SOC according to temperature change (AC vs. DC parameters). (a) AC R_1 Parameter. (NCM523) vs. DC R_1 Parameter (NCM523). (b) AC R_2 Parameter (NCM523) vs. DC R_2 Parameter (NCM523). (c) AC C_2 Parameter (NCM523) vs. DC C_2 Parameter (NCM523). (d) AC R_1 Parameter (NCM622) vs. DC R_1 Parameter (NCM622). (e) AC R_2 Parameter (NCM622) vs. DC R_2 Parameter (NCM622). (f) AC C_2 Parameter (NCM622) vs. DC C_2 Parameter (NCM622).

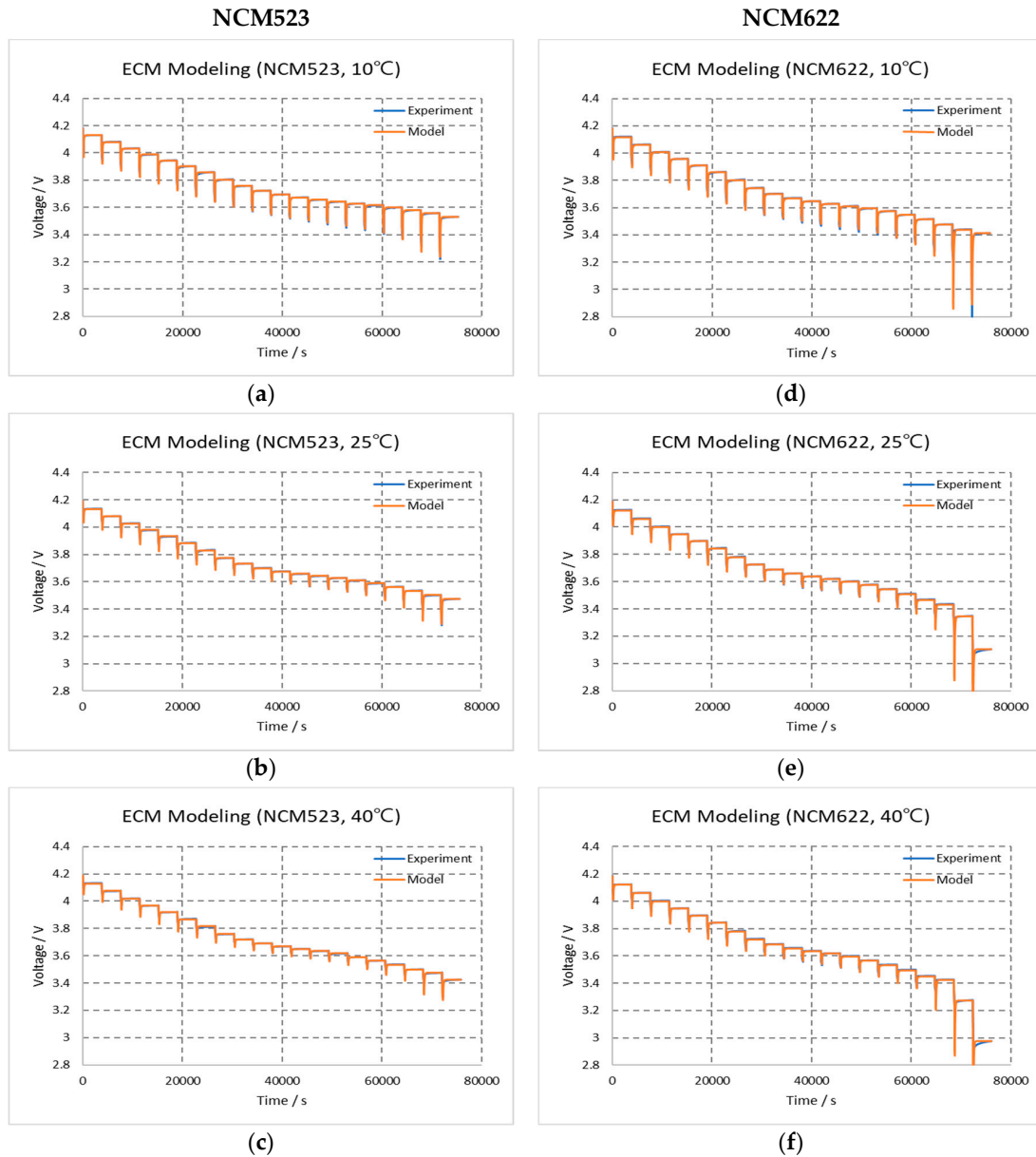


Figure 20. Experimental data vs. modeling results. (a) NCM523 exp. (10 °C) vs. model (b) NCM523 exp. (25 °C) vs. model. (c) NCM523 exp. (40 °C) vs. model (d) NCM622 exp. (10 °C) vs. model. (e) NCM622 exp. (25 °C) vs. model (f) NCM622 exp. (40 °C) vs. model.

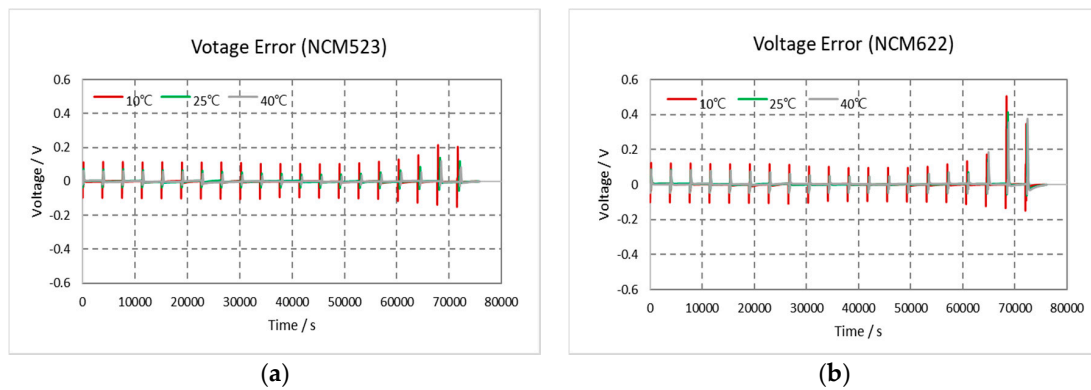


Figure 21. Voltage error (10 °C vs. 25 °C vs. 40 °C): (a) NCM523; (b) NCM622.

4. Conclusions

Various experiments were conducted and analyzed using NCM LIB (NCM523, NCM622) with different Ni contents. Battery characteristics and their dependence on the composition ratio of Ni, Co, and Mn were discussed. The performances of NCM622 and NCM523 were then analyzed through performance experiments using the C-rate. The maximum output power and resistance of NCM622 and NCM523 were calculated and analyzed through HPPC experiments. Accelerated degradation experiments were carried out on the lifetime characteristics. AC impedance characteristics at various SOC values were then analyzed through EIS experiments. The parameters of the battery equivalent circuit were estimated through AC/DC impedance, and the battery model was confirmed by applying the appropriate parameters.

Author Contributions: S.-J.K. and J.-H.C. and J.-H.L. and S.-E.L. conceived and designed the experiment; S.-J.K. and J.-H.C. performed the experiment; visualization, S.-J.K. and J.-H.C.; J.-H.C. and S.-J.K. analyzed the theory; S.-J.K. and J.-H.C. wrote the manuscript; J.-H.C. and J.-H.K. participated in research plan development and revised the manuscript.; supervision J.-H.C. and J.-H.K.; All authors contributed to the manuscript.

Funding: This work was supported by the National Research Foundation of Korea (NRF) grant funded by the Korea government (MSIT) (No. NRF-2018R1C1B6004482) and was supported by the projects of the Korea Electric Power Corporation (R15EA02).

Conflicts of Interest: The authors declare no conflicts of interest.

References

- Choi, J.H. *Understanding Electric Energy Storage Devices (Lithium Secondary Battery)*; Korea Electric Power Corporation Research Institute: Daejeon, Korea, 2014.
- SNE Research. *Lithium Ion Battery Cathode Technology Trend and Market Forecast*; SNE Research: SeongNam, Korea, 2017.
- Julien, C.M.; Mauger, A.; Zaghbi, K.; Groult, H. Comparative Issues of Cathode Materials for Li-Ion Batteries. *Inorganics* **2014**, *2*, 132–154. [[CrossRef](#)]
- Nitta, N.; Wu, F.; Lee, J.T.; Yushin, G. Li-ion battery materials: Present and future. *Mater. Today* **2015**, *18*, 252–264. [[CrossRef](#)]
- International Electrotechnical Commission. *Electric Energy Storage Device*; International Electrotechnical Commission: Geneva, Switzerland, 2016.
- Gummow, R.J.; Liles, D.C.; Thackeray, M.M. Spinel versus layered structures for lithium cobalt oxide synthesised at 400 °C. *Mater. Res. Bull.* **1993**, *28*, 235. [[CrossRef](#)]
- Gummow, R.J.; Thackeray, M.M.; David, W.I.F.; Hull, S. Structure and electrochemistry of lithium cobalt oxide synthesised at 400 °C. *Mater. Res. Bull.* **1992**, *27*, 327. [[CrossRef](#)]
- Delmas, C.; Saadouni, I. Electrochemical and physical properties of $\text{Li}_x\text{Ni}_{1-y}\text{Co}_y\text{O}_2$ phases. *Solid State Ion.* **1992**, *53–56*, 370–375. [[CrossRef](#)]
- Rougier, A.; Saadouni, I.; Gravereau, P.; Willmann, P.; Delmas, C. Effect of cobalt substitution on cationic distribution in Li electrode materials. *Solid State Ion.* **1996**, *90*, 83–90. [[CrossRef](#)]
- Julien, C.; El-Farh, L.; Rangan, S.; Massot, S. Synthesis of $\text{LiNi}_{1-y}\text{Co}_y\text{O}_2$ cathode materials prepared by a citric acid-assisted sol-gel method for lithium batteries. *J. Sol-Gel Sci. Technol.* **1999**, *15*, 63–72. [[CrossRef](#)]
- Li, W.; Curie, J. Morphology effects on the electrochemical performance of $\text{LiNi}_{1-x}\text{Co}_x\text{O}_2$. *J. Electrochem. Soc.* **1997**, *144*, 2773–2779. [[CrossRef](#)]
- Kwon, S.J.; Park, E.Y.; Lim, J.H.; Choi, J.H.; Kim, J.H. Performance Analysis and Degradation Characteristics of NCM LIB for ESS. *Power Electron. Soc.* **2018**, *7*, 219–221.
- Noh, H.J. Comparison of the structural and electrochemical properties of layered $\text{Li}[\text{Ni}_x\text{Co}_y\text{Mn}_z]\text{O}_2$ ($x = 1/3, 0.5, 0.6, 0.7, 0.8$ and 0.85) cathode material for lithium-ion batteries. *J. Power Sources* **2013**, *233*, 121–130. [[CrossRef](#)]
- Yun, J.Y.; Yu, G.; Kook, K.S.; Rho, D.H.; Chang, B.H. SOC-based Control Strategy of Battery Energy Storage System for Power System Frequency Regulation. *Korean Inst. Electr. Eng.* **2014**, *5*, 622–628.
- Jiang, L.; Wang, Q.; Suna, J. Electrochemical performance and thermal stability analysis of $\text{LiNi}_x\text{Co}_y\text{Mn}_z\text{O}_2$ cathode based on a composite safety electrolyte. *J. Hazard Mater.* **2018**, *351*, 260–269. [[CrossRef](#)] [[PubMed](#)]

16. Sun, Y.K.; Chen, Z.; Noh, H.J.; Lee, D.J.; Jung, H.G.; Ren, Y.; Wang, S.; Yoon, C.S.; Myung, S.T.; Amine, K. Nanostructured high-energy cathode materials for advanced lithium batteries. *Nat. Mater.* **2012**, *11*, 942. [[CrossRef](#)] [[PubMed](#)]
17. Jung, R.; Metzger, M.; Magli, F.; Stinner, C.; Gasteigera, H.A. Oxygen Release and Its Effect on the Cycling Stability of $\text{LiNi}_x\text{Mn}_y\text{Co}_z\text{O}_2$ (NMC) Cathode Materials for Li-Ion Batteries. *J. Electrochem. Soc.* **2017**, *164*, A1361–A1377. [[CrossRef](#)]
18. Pan, C. Influences of transition metal on structural and electrochemical properties of $\text{Li}[\text{Ni}_x\text{Co}_y\text{Mn}_z]\text{O}_2$ ($0.6 \leq x \leq 0.8$) cathode materials for lithium-ion batteries. *Trans. Nonferrous Met. Soc. China* **2016**, *26*, 1396–1402. [[CrossRef](#)]
19. Yang, D.; Xu, J.; Jing, X.; Wu, N.; Tian, W. Design of a High Power Battery Based on an Analysis of Data Captured from a Commercial Hybrid Electric Vehicle Running at Operating-Mode Conditions. *Int. J. Electrochem. Sci.* **2015**, *10*, 1940–1952.
20. Stroe, D.I.; Swierczynski, M.; Stroe, A.I.; Knudsen Kær, S. Generalized Characterization Methodology for Performance Modelling of Lithium-Ion Batteries. *Batteries* **2016**, *2*, 37. [[CrossRef](#)]
21. Shim, J.; Striebel, K.A. Characterization of High-Power Lithium-Ion Cells During Constant Current Cycling. *J. Power Sources* **2003**, *122*, 188–194. [[CrossRef](#)]
22. Ma, Z.; Jiang, J.; Shi, W.; Zhang, W.; Mi, C.C. Investigation of path dependence in commercial lithium-ion cells for pure electric bus applications: Aging mechanism identification. *J. Power Sources* **2015**, *274*, 29–40. [[CrossRef](#)]
23. Grossi, M.; Riccò, B. Electrical impedance spectroscopy (EIS) for biological analysis and food characterization: A review. *J. Sens. Sens. Syst.* **2017**, *6*, 303–325. [[CrossRef](#)]
24. Jiménez Gordon, I.A.; Grugeon, S.; Takenouti, H.; Tribollet, B.; Armand, M.; Davoisne, C.; Débart, A.; Laruelle, S. Electrochemical Impedance Spectroscopy response study of a commercial graphite-based negative electrode for Li-ion batteries as function of the cell state of charge and ageing. *Electrochim. Acta* **2017**, *223*, 63–73. [[CrossRef](#)]
25. Schmitt, J.; Maheshwari, A.; Heck, M.; Lux, S.; Vetter, M. Impedance change and capacity fade of lithium nickel manganese cobalt oxide-based batteries during calendar aging. *J. Power Sources* **2017**, *353*, 183–194. [[CrossRef](#)]
26. Plett, G.L. *Battery Management Systems-Volume1, Battery Modeling*; Artech House: Norwood, MA, USA, 2015.
27. de Hoog, J.; Jaguemont, J.; Nikolian, A.; Van Mierlo, J.; Van Den Bossche, P.; Omar, N. A combined thermo-electric resistance degradation model for nickel manganese cobalt oxide based lithium-ion cells. *Appl. Therm. Eng.* **2018**, *135*, 54–65. [[CrossRef](#)]
28. He, Z.; Yang, G.; Lu, L. A Parameter Identification Method for Dynamics of Lithium Iron Phosphate Batteries Based on Step-Change Current Curves and Constant Current Curves. *Energies* **2016**, *9*, 444. [[CrossRef](#)]
29. Jackey, R.; Saginaw, M.; Sanghvi, P.; Gazzarri, J. *Battery Model Parameter Estimation Using a Layered Technique: An Example Using a Lithium Iron Phosphate Cell*; The MathWorks: Natick, MA, USA, 2013.
30. Rahmoun, A.; Biechl, H. Modelling of Li-ion batteries using equivalent circuit diagrams. *Electrotech. Rev.* **2012**, *88*, 152–156.

